Phonon scattering limited mobility in the representative cubic perovskite semiconductors SrGeO_{3}, BaSnO_{3}, and SrTiO_{3}

Christian A. Niedermeier, Yu Kumagai, Keisuke Ide, Takayoshi Katase, Fumiyasu Oba, Hideo Hosono, and Toshio Kamiya

Phys. Rev. B **101**, 125206 — Published 24 March 2020

DOI: 10.1103/PhysRevB.101.125206

Phonon scattering limited mobility in the representative cubic perovskite semiconductors $SrGeO_3$, $BaSnO_3$ and $SrTiO_3$

Christian A. Niedermeier,[1,*] Yu Kumagai,[1] Keisuke Ide,[1] Takayoshi Katase,[1] Fumiyasu Oba,[1,2,] Hideo Hosono,[1,2] and Toshio Kamiya[1,2]

**Corresponding author: c-niedermeier@mces.titech.ac.jp*

[1]Laboratory for Materials and Structures, Tokyo Institute of Technology, Yokohama 226-8503, Japan

[2]Materials Research Center for Element Strategy, Tokyo Institute of Technology, Yokohama 226-8503, Japan

Keywords: cubic perovskite $SrGeO_3$, single crystal growth, optical phonon scattering, electron mobility

Abstract: Cubic perovskite oxides are emerging high mobility transparent conducting oxides (TCOs), but Ge-based TCOs had not been known until the discovery of metastable cubic $SrGeO_3$. $0.5 \times 0.4 \times 0.2$ mm^3 large single crystals of the cubic $SrGeO_3$ perovskite were successfully synthesized employing the high-pressure flux method. The phonon spectrum is determined from the IR optical reflectance and Raman scattering analysis to evaluate the electron transport governed by optical phonon scattering. A calculated room-temperature mobility in the order of 3.9×10^2 $cm^2V^{-1}s^{-1}$ is obtained, identifying cubic $SrGeO_3$ as one of the most promising TCOs. Employing classical phonon theory and a combined experimental-theoretical approach, a comprehensive analysis of the intrinsic electron mobility in the cubic perovskite semiconductors $SrGeO_3$, $BaSnO_3$ and $SrTiO_3$ is provided based on the magnitude of polarization and eigenfrequency of optically active phonons.

I. INTRODUCTION

TCOs are emerging materials combining high electrical conductivity and optical transparency in the visible spectral region, and present important applications in optoelectronic devices. Since the discovery of the high-mobility two-dimensional electron gas in oxide heterostructures,[1] perovskites became particularly attractive for advanced semiconductor technology as they facilitate a new design of future electronic devices due to the unique physics occurring at the interfaces of hetero-junctions.[2] The recent reports of the remarkably high electron mobility at cryogenic temperatures in La:$SrTiO_3$ epitaxial films (>50000 $cm^2V^{-1}s^{-1}$)[3,4] and at room temperature (RT) in La:$BaSnO_3$ single crystals (320 $cm^2V^{-1}s^{-1}$)[5,6] sparked significant interest in understanding the fundamentals of the intrinsic electron transport in perovskites and their application in heterostructures.[7–9]

The discovery of the first Ge-based TCO, cubic perovskite $SrGeO_3$,[10] invites for the exploration of a new promising, emerging material for application in electronics. The large conduction band (CB) dispersions in the main group element cubic perovskites $SrGeO_3$ and $BaSnO_3$ originate from the regular octahedral coordination of the Ge^{4+} (Sn^{4+}) cation to O^{2-} anions with the point symmetry O_h.[11,12] This coordination symmetry prohibits the hybridization of Ge 4s (Sn 5s) and O 2p orbitals at the Γ point in the Brillouin zone. Thus, the resulting non-bonding state at the Γ point and the anti-bonding states at the boundaries of the Brillouin zone have energy levels separated by several eV. The large CB curvatures yield small effective masses of $SrGeO_3$ (0.22 m_e) and $BaSnO_3$ (0.19 m_e),[13,14] where m_e denotes the electron rest mass.

The relatively large static dielectric permittivity of perovskites is a benefical material property which screens the electron-charge interaction and promotes the electron transport. It results from the strongly ionic character of the chemical bonds and the ion displacement from the equilibrium lattice sites. These thermally activated lattice vibrations, known as phonons, may account for a large ionic polarization even when the material is composed of only main group elements. The static dielectric constants of $SrGeO_3$ (18 ± 1) and $BaSnO_3$ (20,[15] 20 ± 2,[16,17] 14.8 ± 0.5[18]) are about 2-3 times larger than those of the well-established TCOs like ZnO ($\varepsilon_s^{\parallel c}$ =7.4, $\varepsilon_s^{\perp c}$ = 8.5),[19] In_2O_3 (ε_s = 8.5)[20] and SnO_2 ($\varepsilon_s^{\parallel c}$ = 14, $\varepsilon_s^{\perp c}$ = 9.0).[21] Although recent Berry phase calculations have revealed that electron transfer has a large contribution to such large

dielectric polarizations, their origins have not yet been discussed in relation to phononic polarizations experimentally. Due to the large polarization, the RT electron mobility in substitutionally doped perovskite oxides is governed by electron-phonon interactions rather than ionized impurity scattering,[22,23] and the dielectric screening of ionized impurities supports a high electron mobility even at enhanced carrier concentrations.[14,24] In contrast to the majority of TCOs with a (n-1)d^{10}ns^0 electronic configuration (n is the principal quantum number), transition metal-based semiconductors such as $SrTiO_3$ and TiO_2 have rather localized unoccupied wave functions originating from the Ti 3d orbitals and a large effective mass. However, these semiconductors may nevertheless exhibit good electrical transport properties. In this case, the large dielectric screening ($SrTiO_3$, ε_s = 310;[25] and TiO_2, $\varepsilon_s^{\parallel c}$ = 173, $\varepsilon_s^{\perp c}$ = 89)[26] is seen as a key property for promoting the electrical conductivity.[27]

This work employs a combined experimental-theoretical approach to provide a fundamental understanding of how the ionic polarization, decoded into the contribution of separate phonon modes, impacts the intrinsic electron transport in cubic perovskites. $SrTiO_3$ and $BaSnO_3$ have been well characterized, and recently, also large-size single $BaSnO_3$ crystals could be grown from the melt[28] and hydrothermal methods.[29] In contrast, up to present, the cubic perovskite $SrGeO_3$ (Fig. 1a) has remained widely unexplored due to the difficulty in the synthesis, requiring high-pressure conditions.[30] So far, only a $0.1 \times 0.08 \times 0.08$ mm^3 small single crystal was obtained employing the high-pressure sintering of a polycrystalline sample.[31] We report the first successful single crystal growth of cubic $SrGeO_3$ employing the high-pressure flux method. The phonon spectrum of cubic $SrGeO_3$ was determined, which allows for a quantitative analysis of the intrinsic mobility, in comparison with $SrTiO_3$ and $BaSnO_3$. We conclude that the particular combination of properties, a large polarization of the hardest longitudinal optical (LO) phonon mode *and* a small effective mass, would be effective for the design of new electronic materials with an exceptionally high RT electron mobility.

II. MATERIALS AND METHODS

A. Experimental

Cubic $SrGeO_3$ single crystals were grown using a belt-type high-pressure apparatus.[32] The precursor powder, monoclinic $SrGeO_3$ (spacegroup *C2/c*), was prepared by calcination of stoichiometric quantities of $SrCO_3$ and GeO_2 at 1100 ^oC for 12 h on Pt foil. The monoclinic $SrGeO_3$ powder (100 mg) was mixed in the 1:7 molar ratio with a $SrCl_2$/NaCl flux of the molar composition 3:2. The eutectic point in the $SrCl_2$-NaCl system lies at 544 ^oC and 53 mol% $SrCl_2$.[33] $SrCl_2$ and NaCl were dehydrated at 350 ^oC prior to the mixing. The powder mixture was filled into a Au capsule, pressed and inserted into a NaCl/ZrO_2 cell of the weight ratio 9:1 with a carbon heater. A 5 GPa pressure was applied and the specimen was annealed at 1100 ^oC for 4 hours, then slowly cooled down to 800 ^oC within 18 h, at which point the heating was turned off and the specimen was water-cooled to room temperature. After washing out the flux with deionized water, yellowish transparent cubic $SrGeO_3$ ($Pm\bar{3}m$) single crystals of up to $0.5 \times 0.4 \times 0.2$ mm^3 size and naturally grown 100 facets were obtained (Fig. 1b). Colorless, orthorhombic β-$SrGe_2O_5$ (*Pnma*) single crystals were obtained as side product.[34] We also prepared dense, cubic $SrGeO_3$ and $La_{0.02}Sr_{0.98}GeO_3$ polycrystalline pellets of 5 mm diameter by sintering the precursor powder in a BN capsule at 1100 ^oC for 2 h at 5 GPa pressure. The pellets were cleaved and the surface was mirror-polished for optical reflectance measurements.

The 100 out-of-plane high-resolution X-ray diffraction (HR-XRD) pattern of cubic $SrGeO_3$ single crystals and the rocking curve of the 200 peak were recorded using a Rigaku SmartLab diffractometer equipped with a monochromatic Cu $K_{\alpha 1}$ X-ray source (1.5406 Å) and utilizing parallel beam optics. Reflection ellipsometry spectra (Jobin Yvon UVISEL) were recorded using IR spectroscopy (Hitachi U-4100) from 1.5–5.0 eV and using vacuum Fourier-transform IR spectroscopy (Bruker Vertex 70v) from 100–8000 cm^{-1} wavenumber. Al and Au mirrors were used as 100% reflectance standard, respectively. For measuring the non-polarized Raman spectrum of cubic $SrGeO_3$ single crystals, we used a Horiba LabRAM HR system in the backscattering configuration using the 457 nm wavelength of a Nd:YVO_4 laser (Cobolt Twist 50) and a liquid N_2-cooled CCD detector.

B. Computational

We performed the theoretical calculations using hybrid density functional theory (DFT) and the projector augmented wave method[35] as implemented in the Vienna Ab initio Simulation Package (VASP).[36,37] As the cubic perovskite has no degree of freedom for internal atomic coordinates, only the lattice parameter *a* was relaxed by using the PBE0 hybrid functional.[38] A plane wave cutoff of 500 eV and a Γ-centered 6 x 6 x 6 *k*-mesh were used. The relaxed ground state cubic $SrGeO_3$ structure has the calculated lattice parameter of 3.80 Å, which is in excellent agreement to the experimental value at room temperature, 3.7978 Å.[31] The electronic band structure was calculated employing maximally localized Wannier functions using the code Wannier90.[39] We employed the PBE0 functional because it gave a reasonable band gap for related oxides, GeO_2 (tetragonal, *$P4_2/mnm$,* E_g^{calc} = 4.55 eV, E_g^{exp}= 4.68 eV)[40] and $BaSnO_3$ (E_g^{calc} = 3.17 eV, E_g^{exp}= 2.95 eV).[24]

We used the phonopy code[41] and adopted the experimental lattice parameters at room temperature since they largely affect the phonon frequencies. For the exchange-correlation functional, we adopted the generalized gradient approximation with a very high accuracy of total energy criteria for self-consistent convergence, 10^{-8} eV. 2 x 2 x 2 40-atom supercells were used along with a plane wave cutoff of 400 eV and a Γ-centered 4 x 4 x 4 *k*-mesh.

III. CRYSTAL QUALITY, ELECTRONIC STRUCTURE AND OPTICAL CHARACTERIZATION OF CUBIC $SrGeO_3$

The 100 out-of-plane HR-XRD pattern of the $SrGeO_3$ single crystal confirms the cubic structure and a 3.7980 Å lattice parameter is obtained using Bragg's law (Fig. 1c). The narrow, 0.023° wide full-width at half maximum (FWHM) of the rocking curve of the 200 peak indicates a low mosaicity of the single crystal (Fig. S1). The PBE0-calculated band structure of the cubic perovskite $SrGeO_3$ shows a 2.7 eV indirect band gap of the CB minimum at the *Γ* point and the valence band (VB) maximum at the *R* point of the first Brillouin zone (Fig. 1d). The effective mass of 0.22 m_e is determined from the CB curvature at the Γ point[42]

$$m_e^* = \hbar^2 \left(\frac{d^2 E}{dk^2} \right)^{-1} \quad (1)$$

where $\hbar$ is the reduced Planck constant and k is the reciprocal space vector. Using a cleaved and mirror-polished cubic $SrGeO_3$ polycrystalline pellet, we obtained the reflection ellipsometry spectrum (Fig. 1e) to evaluate the absorption coefficient α. Note that the absorption below the optical band gap is a measurement artefact due to the residual surface roughness which causes diffuse scattering or trace sub-gap absorption from in-band gap defects. The linear fits to the $\alpha^{1/2}$ and α^2–photon energy plots in the vicinity of the absorption edge allow for determination of 2.7 and 3.4 eV optical indirect and direct band gaps, respectively, in agreement with the specular reflectance edge and the calculated values (Fig. 1f).

IV. PHONON SPECTRA OF CUBIC PEROVSKITES

A. IR dispersion function of cubic $SrGeO_3$

To investigate the intrinsic electron mobility in cubic $SrGeO_3$, we first determine the phonon spectrum. Materials crystallizing in the cubic perovskite structure (one $SrGeO_3$ chemical unit) have a total of 15 phonon modes;[43] 3 acoustic modes, 4 pairs of doubly degenerate transverse optical (TO) modes and 4 longitudinal optical (LO) phonon modes. Only 3 of the 4 pairs of optical modes are IR active, having a net ionic dipole moment which contributes to the macroscopic static polarization. Thus, we construct the optical dispersion model using a Lorentz oscillator[44] for each of the three IR active TO phonon modes,

$$\varepsilon(\omega) = \varepsilon_\infty + \sum_\mu \frac{\varepsilon_{t_\mu} \omega_{t_\mu}^2}{\omega_{t_\mu}^2 - \omega^2 - i\gamma_\mu \omega} \quad (2)$$

where ε_∞ is the high-frequency dielectric constant, ω_{t_μ} is the TO phonon eigenfrequency and γ_μ is the damping frequency, both given as angular frequencies. The contribution of the individual phonon modes to the static polarization is given by the TO phonon oscillator strength ε_{t_μ}. Following the classical theory of polarization waves in crystals,[45] the TO phonon oscillator strength is given by

$$\varepsilon_{\mathrm{t_\mu}} = \frac{(\sum_i e_i^* x_{\mathrm{t_u}i})^2}{\omega_{\mathrm{t_\mu}}^2 \varepsilon_0 V \sum_i M_i x_{\mathrm{t_u}i}^2} \quad (3)$$

where ε_0 is the vacuum permitivity and V is the unit cell volume. The ionic polarization results from the displacement $x_{\mathrm{t_\mu}i}$ of ions with the Born effective charge e_{i}^* and the atomic mass M_{i}. This classical theory holds for the harmonic vibration regime, in which ion displacements are sufficiently small, such that the induced polarization can be described as a linear function of $x_{\mathrm{t_\mu}i}$. In fact, the displacement of a certain ion would also induce a polarization on other ions as well, giving a rather complicated description of the total polarization.

For the determination of the dispersion parameters in Eq. (2), we fit the specular IR reflectance spectrum of a mirror-polished cubic $SrGeO_3$ polycrystalline pellet (Fig. 2a). In addition, we measured the Raman spectrum for a cubic $SrGeO_3$ single crystal. The first-order Raman peaks provide the LO phonon frequencies, which are given by the maxima of the loss function $-\mathrm{Im}(\varepsilon^{-1})$.[46] According to theory, cubic perovskites shall not show any first-order Raman active modes,[43] but we observe the LO_2 and LO_3 phonons at 493 cm^{-1} and 742 cm^{-1} wavenumber, respectively, as well as their overtones at 995 cm^{-1} and 1484 cm^{-1} (Fig. 2b). The shoulder peak at 695 cm^{-1} may relate to the LO_1 + LO_2 overtone. The LO_1 mode can not be identified due to its negligibly small polarization. The Raman spectrum of cubic $BaSnO_3$ is strikingly similar to that of cubic $SrGeO_3$, and a large scattering intensity of the LO_2 and LO_3 phonons is observed. The large Raman response of LO modes has been attributed to resonant multi-phonon scattering known to occur in materials of large lattice polarizability.[16]

The IR reflectance spectrum was fitted by first constraining the LO_2 and LO_3 frequencies to 493 cm^{-1} and 792 cm^{-1}, respectively, and determining the high-frequency dielectric constant ε_∞= 4.2 $\pm$ 0.2 from the position of the reflectance edge near a frequency of 760 cm^{-1}. Then, all dispersion parameters were allowed to vary for the final fitting to obtain a reliable dispersion model which can very well reproduce both, the IR reflectance spectrum and the frequencies of the first-order LO_2 and LO_3 Raman peaks. We do not attempt to fit the Raman scattering intensity, which is a complicated function of wavenumber that cannot be simply described by considering only the loss function $-\mathrm{Im}(\varepsilon^{-1})$.[47] The fitting was performed using the RefFIT

program[48] and the obtained dispersion parameters are given in Table 1. The cubic $SrGeO_3$ static dielectric constant ε_s = 18 $\pm$ 1 is obtained from the sum of the high-frequency dielectric constant and all three TO phonon oscillator strengths ε_{t_μ}. The largest contribution to the total static polarization originates from the TO_2 mode ($\varepsilon_{t_2} = 11.2$).

The result of our dispersion model contradicts the finding of the apparently very high static dielectric constant (ε_s = 114) and largely polar TO_1 mode (ε_{t_1} = 100.5) in cubic $SrGeO_3$ reported by Grzechnik.[49–51] Our experimental results are further supported by the agreement with the theoretical calculation of the cubic $SrGeO_3$ static dielectric constant $\varepsilon_s^{\mathrm{calc}} = 21$ using density functional pertubation theory.[52] Moreover, it is reasonable that the cubic $SrGeO_3$ dispersion parameters are comparable to those reported for $BaSnO_3$ (ε_s = 20,[15] 20 $\pm$ 2,[16,17] 14.8 $\pm$ 0.5[18]), due to the similarities in the chemical bonding and electronic structure. We also calculated the high-frequency dielectric constant $\varepsilon_\infty^{\mathrm{calc}} = 4.9$ of cubic $SrGeO_3$, which is slightly larger as compared to the experimental value.

Table 1: TO phonon frequency ω_{t_μ}, damping frequency γ_μ and oscillator strength ε_{t_μ} describing the $SrGeO_3$, $BaSnO_3$ and $SrTiO_3$ IR dielectric functions using three Lorentz oscillators (Eq. 1). The high-frequency dielectric constants are $\varepsilon_\infty^{\mathrm{SrGeO3}} = 4.2 \pm 0.2$, $\varepsilon_\infty^{\mathrm{BaSnO3}} = 4.3$[16] and $\varepsilon_\infty^{\mathrm{SrTiO3}} = 5.2$.[25] Values in brackets denote calculation results using the PBE functional. The theoretical TO phonon oscillator strength ε_{t_μ} is obtained from the phonon calculation results of the ion displacement vectors and Born effective charges (Eq. (3)).

Material	Eigenfrequency ω_{t_μ} (cm^{-1})	Energy $\hbar\omega_{t_\mu}$ (meV)	Damping frequency γ_μ (cm^{-1})	Oscillator strength ε_{t_μ} -
$SrGeO_3$	189 (180)	23	4.0	1.8 (3.1)
	291 (270)	36	7.6	11.2 (9.8)
	634 (671)	79	39	0.83 (1.4)
$BaSnO_3$[a)]	135 (136)	17	10	3.8 $\pm$ 2 (3.8)
	246 (231)	30	18	10.8 (13.8)
	629 (641)	78	26	0.76 (1.0)
$SrTiO_3$[b)]	88 (81)	11	26	299 (288)
	178 (173)	22	6.1	3.6 (21)
	546 (561)	68	27	1.9 (2.9)

[a)]References[16,17]; [b)]Reference[25]

B. LO phonon oscillator strength

The LO phonon oscillator strength ε_{l_ν} is calculated from the dispersion model parameters, after expansion of the longitudinal mode displacements x_{l_ν} in terms of those of the transverse modes x_{t_μ},[53] according to

$$\varepsilon_{l_\nu} = \varepsilon_\infty^2 \left(\omega_{l_\nu}^2 \sum_\mu \frac{\varepsilon_{t_\mu} \omega_{t_\mu}^2}{(\omega_{l_\nu}^2 - \omega_{t_\mu}^2)^2} \right)^{-1} \tag{4}$$

with the results given in Table 2. The matrix elements of Eq. (4) describe the coupling strength between TO and LO modes (Table 3).

Table 2: LO phonon frequency ω_{l_ν}, LO phonon oscillator strength $\varepsilon_{\mathrm{l}_\nu}$ for $SrGeO_3$, $BaSnO_3$ and $SrTiO_3$. Values in brackets denote calculation results using the PBE functional. The theoretical LO phonon oscillator strength $\varepsilon_{\mathrm{l}_\mu}$ is obtained from the phonon calculation results of the ion displacement vectors and Born effective charges (Eq. (3)). The polaron coupling constant α_ν and RT relaxation time τ_ν^{RT} is calculated according to Eqs. (5) and (6), respectively.

Material	Eigenfrequency ω_{l_ν}	Energy $\hbar\omega_{\mathrm{l}_\nu}$	Oscillator strength $\varepsilon_{\mathrm{l}_\nu}$	Coupling constant $\alpha_\nu\left(\frac{m_\mathrm{e}}{m_\mathrm{e}^*}\right)^{1/2}$	RT relax. time τ_ν^{RT}
	(cm^{-1})	(meV)	-	-	(10^{-14} s)
$SrGeO_3$	196 (191)	24	0.047 ± 0.01 (0.09)	0.062	72
	493 (426)	61	1.4 ± 0.2 (1.9)	1.2	7.5
	748 (791)	93	1.8 ± 0.2 (1.4)	1.2	17
$BaSnO_3$	146 [a] (148)	18	0.11 ± 0.07 (0.15)	0.17	25
	425 [a] (370)	53	1.9 ± 0.1 (2.1)	1.6	4.4
	720[a] (726)	89	1.4 ± 0.1 (1.3)	0.92	24
$SrTiO_3$	174 (154)	22[b]	0.02 (0.08)	0.017[b]	89
	461 (438)	57[b]	0.94 (1.7)	0.54[b]	4.8
	816 (807)	101[b]	4.2 (1.6)	1.8[b]	2.8

[a] Reference[16]; [b] cf. reference[54].

Table 3: The matrix elements of Eq. (4) describe the strength of coupling between TO and LO phonon modes, from which the LO phonon oscillator strength ε_{l_ν} is obtained.

Material		$\omega_{l_\mu}^2 \frac{\varepsilon_{t_\mu}\omega_{t_\mu}^2}{\left(\omega_{l_\nu}^2-\omega_{t_\nu}^2\right)^2}$			$\omega_{l_\mu}^2 \sum_\mu \frac{\varepsilon_{t_\mu}\omega_{t_\mu}^2}{\left(\omega_{l_\nu}^2-\omega_{t_\nu}^2\right)^2}$
	ν	$\mu = 1$	$\mu = 2$	$\mu = 3$	
$SrGeO_3$	1	364	17.1	0.1	381
	2	0.4	9.2	3.2	12.8
	3	0.1	2.4	7.5	10.0
$BaSnO_3$	1	154	9.1	0.1	163
	2	0.5	8.1	1.3	9.9
	3	0.1	1.6	11.7	13.4
$SrTiO_3$	1	1367	1372	0.2	1510
	2	11.6	0.7	16.4	28.7
	3	3.5	0.2	2.8	6.5

C. Phonon spectra of the cubic perovskites $SrGeO_3$, $BaSnO_3$ and $SrTiO_3$

In Fig. 3 we provide the IR dispersion functions of cubic $SrGeO_3$ in comparison with $BaSnO_3$ and $SrTiO_3$, which were determined by optical analyses of single crystals.[16,17,25] The maxima of the imaginary part ε_2 of the dielectric function provide the TO phonon frequencies ω_{t_μ}. The maxima of the loss function $-\mathrm{Im}(\varepsilon^{-1})$ provide the LO phonon frequencies ω_{l_ν}, which correspond to the zeros of the real part ε_1. The peak heigths of the TO and LO phonons indicate the magnitude of polarization, but it must be considered that the peak broading due to damping ($\gamma_\mu > 0$) is taken into account. The phonon spectra of $SrGeO_3$ and $BaSnO_3$ are very similar, and both materials show large polarizations for the TO_2, LO_2 and LO_3 modes (Fig. 3b). However, the $SrGeO_3$ eigenfrequencies of these modes are noticeably shifted to higher frequencies. The $SrTiO_3$ phonon spectrum is distinctly different and shows a remarkably large polarization of the TO_1 and LO_3 modes.

To understand the differences in the phonon spectra between cubic $SrGeO_3$ and $BaSnO_3$, and $SrTiO_3$ on the other hand, we calculated the phonon band structures and displacement vectors of all eigenmodes (Fig. 4). The $SrGeO_3$ and $SrTiO_3$ phonon band structures show imaginary frequencies at the Brillouin zone boundaries, because at ambient pressure and absolute zero temperature, the thermodynamically stable crystal structures are not cubic ($Pm\bar{3}m$), but monoclinic ($C2/c$) and tetragonal ($I4/mcm$),[55] respectively. The 3 IR active TO eigenmodes in $SrGeO_3$ and $BaSnO_3$ are very similar, and one schematic is given to illustrate these modes in both materials. There are different displacement vectors for the following ions: A^{2+} and B^{4+} cations, and $O_{||}^{2-}$ and $2\times O_{\perp}^{2-}$ anions with displacements vectors parallel and perpendicular to the axis of the B—O bond, respectively.

Despite having the same cubic perovskite crystal structure, the $SrTiO_3$ eigenvectors are distinctly different from those of $SrGeO_3$ and $BaSnO_3$. For example, the displacements of the TO_1 mode depend on the electronic structure and whether the B^{4+} cation valence orbitals are comprised of Ge 4s (Sn 5s) or Ti 3d orbitals. In $SrGeO_3$ ($BaSnO_3$), the Ge^{4+} (Sn^{4+}) cation is displaced along the $Ge^{4+}-O_{||}^{2-}$ ($Sn^{4+}-O_{||}^{2-}$) bond axis and as part of the GeO_6 (SnO_6) octahedron in the same direction as the $O_{||}^{2-}$ and $O_{\perp}^{2-}$ anions (Fig. 4b). This is in contrast to the TO_1 mode in $SrTiO_3$, for which the Ti^{4+} cations and the $O_{||}^{2-}$ anions of the TiO_6 octahedron are displaced in opposite directions (Fig. 4c). The variation of the $Ti^{4+}-O_{||}^{2-}$ bond length compresses the bonding O 2p orbital and increases its d character.[56] The dynamic charge transfer from $O_{||}^{2-}$ to Ti^{4+} ions results in anomalously large Born effective charges $e^*_{O_{||}}$ and e^*_{Ti} (Table 4). Consequently, the TO_1 mode polarization in $SrTiO_3$ is excessively large, which gives rise to a pronounced TO-LO splitting and a strikingly large LO_3 polarization.

Table 4: Calculated Born effective charge e^* (in units of the electron charge e) of ions in $SrGeO_3$, and $BaSnO_3$ and $SrTiO_3$ from density functional pertubation theory.

Material	e^*_{A}	e^*_{B}	$e^*_{\mathrm{O}_{\parallel}}$	$e^*_{\mathrm{O}_{\perp}}$
$SrGeO_3$	2.6	4.5	-3.7	-1.7
$BaSnO_3$	2.7	4.4	-3.3	-1.9
$SrTiO_3$	2.5	7.7	-6.1	-2.1

We do not consider the triply degenerate, IR inactive eigenmode any further, which is characterized by the displacement of two $O^{2-}_{\perp}$ ions in opposite directions without a net ionic dipole moment (Fig. S3). The calculation data of eigenmodes at various points in the phonon band structures is provided as supplementary material for interactive visualization of ion displacements using the website of Miranda.[57] Our results for the $BaSnO_3$ and $SrTiO_3$ eigenmodes agree with a recent phonon calculation,[58] and the analyses of experimental dispersion data obtained from single crystals,[25,59] respectively.

V. LO PHONON SCATTERING

A. Determination of the scattering limited electron mobility

In all cubic perovskites of this study, the LO_1 phonon polarization is negligibly weak. Thus, the electron-phonon interaction is governed by the large polarization of the LO_2 and LO_3 phonons. We describe the electron-phonon interaction quantitatively by polaron coupling constants α_ν according to[53,60]

$$\alpha_\nu = \frac{1}{8\pi\varepsilon_0}\frac{e^2}{r_p \hbar\omega_{\mathrm{l}_\nu}}\left(\frac{1}{\varepsilon_\infty}-\frac{1}{\varepsilon_\mathrm{s}}\right)\frac{\varepsilon_{\mathrm{l}_\nu}}{\sum_\nu \varepsilon_{\mathrm{l}_\nu}} \tag{5}$$

where e is the electron charge and $r_p = \left(\hbar/2m^*_\mathrm{e}\omega_{\mathrm{l}_\nu}\right)^{1/2}$ is the polaron radius. The polaron binding energy $\alpha_\nu\hbar\omega_{\mathrm{l}_\nu}$ as derived by Fröhlich[60] is shown to be valid for weak coupling interactions ($\alpha_\nu < 10$). Fröhlich's model was extended to describe the coupling constants of materials having more than one optical phonon mode, by weighting them according to their phonon oscillator strength, as given by the term $\varepsilon_{\mathrm{l}_\nu}/\sum_\nu \varepsilon_{\mathrm{l}_\nu}$.[53] The electron-phonon coupling is

weak when I) the effective mass m_e^* is small, II) the high-frequency dielectric constant ε_∞ is large to promote screening of the polarization, and III) the oscillator strength ε_{l_ν} of the LO phonon mode is weak. The polaron coupling constants α_ν for all LO phonon modes are summarized in Table 2.

The LO phonon energy $\hbar\omega_{l_\nu}$ and the coupling parameter α_ν determine the relaxation time τ_ν of momentum loss by carrier scattering due to electron-LO phonon interactions. It is calculated for each of the LO phonon modes according to[61]

$$\tau_\nu = \frac{1}{2\alpha_\nu\omega_{l_\nu}}\left(\frac{m_e^*}{m_p}\right)^2 f(\alpha_\nu)\left[\exp\left(\frac{\hbar\omega_{l_\nu}}{k_B T}\right) - 1\right] \quad (6)$$

where k_B is the Boltzmann constant, T is the absolute temperature and $f(\alpha_\nu)$ is a dimensionless function, slowly increasing from 1.0 to 1.2 for $0 < \alpha_\nu < 3$. The polaron mass $m_p = (1 + \alpha_\nu/6)m_e^*$[44] describes the larger effective mass of an electron which creates a local polarization due to the Coulombic interaction with the ions of the crystal. Eq. (6) for the relaxation time is valid for temperatures smaller than the Debye temperature ($T \ll \hbar\omega_{l_\nu}/k_B$). This condition is satisfied at RT for all considered phonon modes with the exception of the soft LO_1 modes, which in any case can be neglected due to their negligibly small polarization.

The relaxation time τ_ν is largely dependent on the LO phonon energy $\hbar\omega_{l_\nu}$ and the oscillator strength ε_{lv} as shown in Fig. 5. In general, a hard LO phonon mode exhibits a large coupling parameter, but the thermal occupation at RT, as given by the term $\exp(-\hbar\omega_{l_\nu}/k_B T)$, is small as compared to soft modes. The smallest relaxation time τ_ν among all LO phonon modes in each material is crucial for the effective relaxation time τ_{LO}, following Mathiessen's rule[53]

$$\tau_{LO} = \left(\sum_\nu \frac{1}{\tau_\nu}\right)^{-1} \quad (7)$$

The electron mobility μ_{LO} is determined from the ratio of effective scattering relaxation time τ_{LO} and effective mass m_e^*, according to[44]

$$\mu_{LO} = \frac{e\,\tau_{LO}}{m_e^*} \quad (8)$$

We calculate the intrinsic RT mobilities for cubic $SrGeO_3$, $BaSnO_3$, and $SrTiO_3$ of 3.9×10^2, 3.0×10^2 and 2×10 $cm^2V^{-1}s^{-1}$, respectively (Table 5).

Table 5: Lattice parameter a, optical and static dielectric constants ε_∞ and ε_s, and effective mass m_e^* of cubic $SrGeO_3$, $BaSnO_3$ and $SrTiO_3$. The effective RT relaxation time τ_{LO}^{RT} and RT electron mobility μ_{LO}^{RT} is calculated according to Eq. (7) and (8), respectively.

Material	Lattice parameter a (Å)	Dielectric constants ε_∞ -	ε_s -	Effective mass m_e^* (m_e)	Effective RT relaxation time τ_{LO}^{RT} (10^{-14} s)	RT electron mobility μ_{LO}^{RT} ($cm^2V^{-1}s^{-1}$)
$SrGeO_3$	3.798[a]	4.2 ± 0.2	18 ± 1	0.22	4.9 ± 0.4	$3.9 \pm 0.5 \times 10^2$
$BaSnO_3$	4.117[b]	4.3[d]	20 ± 2[d]	0.19 ± 0.02[f]	3.2 ± 0.3	$3.0 \pm 0.6 \times 10^2$
$SrTiO_3$	3.905[c]	5.2[e]	310[e]	1.8[g]	1.7	2×10

[a] Reference[31]; [b] Reference[62]; [c] Reference[63]; [d] References[16,17]; [e] Reference[25]; [f] Reference[14]; [g] Reference[64]

The uncertainties in the determination of the high-frequency dielectric constant ε_∞, the electron effective mass m_e^* and the LO phonon oscillator strength ε_{l_ν} are the critical parameters for the error in determining the electron mobility. The combined evaluation of the IR reflectance and Raman scattering of cubic $SrGeO_3$ presented in this study allows for a very reliable determination of both, phonon energies and oscillator strengths. Therefore, the resulting error of the mobility calculation from these parameters is comparably small. Despite the experimental uncertainty, the present method for calculating the electron mobility is powerful from the viewpoint of providing a very intuitive understanding of how individual phonon modes contribute to the effective relaxation time. In addition, it allows to circumvent the large computational effort of DFT calculations. Furthermore, theoretical papers on DFT calculations of the phonon scattering-limited mobility often adopt experimental values such as the effective mass, dielectric constants and phonon energies as input parameters, without consideration of the experimental error. Thus, the rather generous tolerance limits of the present calculation results shall not be surprising.

B. Differences between the phonon spectra and implications for the scattering relaxation time

1. $SrGeO_3$ and $BaSnO_3$

In both materials, $SrGeO_3$ and $BaSnO_3$, the LO_2 phonon mode is the most crucial one for the scattering (Fig. 5). This mode is described by a vibration of the Ge^{4+} (Sn^{4+}) cation against the two $O_{\perp}^{2-}$ anions in the equatorial positions of the GeO_6 (SnO_6) octahedron, while the displacement vectors of Sr^{2+} (Ba^{2+}) and $O_{||}^{2-}$ are comparably small (cf. Fig. 4b). Considering only the displacement of Ge^{4+} (Sn^{4+}) and $O_{\perp}^{2-}$ ion sublattices, and regarding other ions are fixed on their equilibrium lattice sites, the phonon eigenfrequency is proportional to the square root of the reduced mass of the Ge^{4+} (Sn^{4+}) and $2\times O_{\perp}^{2-}$ ions[44]

$$\omega_{t_\mu}^2 = 2k_\mu \left(\frac{1}{M_\alpha} + \frac{1}{M_\beta}\right) \tag{9}$$

as follows from the analogy to the case of a diatomic crystal. Here, M_α and M_β denote the mass of the ions in the two ion sublattices and k_μ is the force constant. Thus, it is concluded that the TO_2 and LO_2 eigenfrequencies in $SrGeO_3$ (291 and 493 cm^{-1}) are increased with respect to the corresponding modes in $BaSnO_3$ (246 and 425 cm^{-1}) due to the smaller atomic mass of Ge (72.6 u) as compared to Sn (118.7 u). The TO_3 eigenfrequencies in $SrGeO_3$ (634 cm^{-1}) and $BaSnO_3$ (629 cm^{-1}) are nearly identical, since they are mainly described by a vibration of only $O_{||}^{2-}$ and $O_{\perp}^{2-}$ anions. As is seen from the expansion coefficient matrix to obtain the LO phonon oscillator strengths (Eq. (4) and Table 3), the increased TO_2 and LO_2 eigenfrequencies in $SrGeO_3$ result in a stronger coupling between the LO_2–TO_3 modes and a weaker coupling between TO_3–LO_3 modes as compared to the corresponding ones in $BaSnO_3$. Thus, the relative LO_2 oscillator strength $\varepsilon_{l_2}/\sum_\nu \varepsilon_{l_\nu}$ in $SrGeO_3$ (1.2/3.2) is comparably smaller than of BaSnO3 (1.9/3.4), resulting in a somewhat longer scattering relaxation time τ_ν (Table 5).

2. $SrTiO_3$

Among the $SrTiO_3$ LO phonons, the hard LO_3 mode exhibits the largest polarization and it is the most crucial one for the intrinsic mobility (Fig. 5c). However, the hard LO_3 mode is the least thermally occupied mode at RT among all three LO modes (cf. Eq. (6)). Considering the large $SrTiO_3$ effective mass of 1.8 m_e, the resulting 17 ps scattering relaxation time is nevertheless

remarkably long, and only by a factor of 2-3 shorter than that obtained for $SrGeO_3$ and $BaSnO_3$ (cf. Table 5).

C. Implications for the design of high RT mobility semiconductors

The results of our analysis provide an important guideline for the design of high RT mobility semiconductors. The most promising candidate materials shall combine both properties, a small effective mass *and* a comparably large polarization for the hardest LO mode. A large static dielectric constant is indicative of a strongly polar TO phonon mode which in turn yields an increased polarization of hard LO modes. Transition metal oxides commonly exhibit a large static dielectric constant due to the dynamic charge transfer between ions and increased Born effective charges, but the compromise is a large effective mass, since d-orbitals are generally more localized than s-orbitals. Thus, it would be very exciting to explore transition metal-based compound semiconductors which, in analogy to $SrGeO_3$ and $BaSnO_3$, show a non-bonding character of the cation-derived CB, and consequently, a reduced effective mass. The recently synthesized tetragonal ZrOS semiconductor with a dispersive CB derived from a Zr 3d non-bonding state and small 0.36 m_e effective mass proves that such materials design is feasible,[65] providing very interesting new candidates for future investigation.

D. Comparison of the calculated mobility with experimental results

The calculation result for $BaSnO_3$ is in very good agreement with experimental values determined by Hall effect measurements of La-doped single crystals (220–320 $cm^2V^{-1}s^{-1}$).[6,28] Furthermore, the calculated RT mobility in the order of 2×10 $cm^2V^{-1}s^{-1}$ for $SrTiO_3$ agrees well with the measured Hall mobility of about 5 $cm^2V^{-1}s^{-1}$ determined for La-doped $SrTiO_3$ epitaxial thin films.[22]

To determine the electrical transport properties in cubic $SrGeO_3$ experimentally, we fit the IR reflectance spectrum of a mirror-polished 2 at.% La-doped $SrGeO_3$ polycrystalline pellet (Fig. 6). At such high doping level, the phonon spectrum is screened due to the large electronic contribution of free carriers to the dielectric function. Thus, the fitting is performed by only using the Drude model,[44]

$$\varepsilon_D(\omega) = \varepsilon_\infty - \frac{\varepsilon_\infty \omega_{\mathrm{p}}^2}{\omega^2 + i\omega/\tau_{\mathrm{p}}} \quad (10)$$

where ω_{p} denotes the unscreened plasma frequency and τ_{p} denotes the carrier scattering relaxation time. We determine the optical mobility of 42 $\pm$ 3 $cm^2V^{-1}s^{-1}$ (Eq. (8)), the carrier concentration of $1.3 \pm 0.1\times10^{20}$ cm^{-3} (Eq. S(1)) and the optical resistivity of $1.1 \pm 0.1\times10^{-3}$ Ωcm^{-1} (Eq. S(2)). The reduced optical mobility as compared to the calculation result may indicate the presence of defects, including the possibility of Ge vacancy formation or a reduction of Ge^{4+} to Ge^{2+}. The Hall effect measurement of substitutionally doped $SrGeO_3$ single crystals will be the subject of further investigation, when crystals of larger size can be grown and characterized.

VI. CONCLUSION

In summary, we have successfully synthesized cubic $SrGeO_3$ perovskite single crystals using the high-pressure flux growth. The optical phonon spectrum is determined from IR optical reflectance and Raman analyses to evaluate the electron transport governed by LO phonon scattering. Employing the classical phonon theory and a combined experimental-theoretical approach, we analysed the individual eigenmodes to gain a fundamental understanding of the similarities and differences in the phonon spectra for the cubic perovskites $SrGeO_3$, $BaSnO_3$ and $SrTiO_3$. Cubic $SrGeO_3$ exhibits a calculated RT mobility in the order of 3.9×10^2 $cm^2V^{-1}s^{-1}$, demonstrating great promise as a high-performance TCO. We suggest a universal guideline for the exploration of new high RT mobility semiconductors. The combined properties of a small effective mass *and* a large polarization of the hardest LO mode is in favor of supporting an exceptionally high RT mobility despite the electron-phonon interactions.

Acknowledgements

We are thankful to Dr T. Stanislavchuk from New Jersey Institute of Technology for sharing the $BaSnO_3$ IR ellipsometry data. The work at Tokyo Institute of Technology was supported by the MEXT Element Strategy Initiative to Form Core Research Center (JPMXP0112101001). C.A.N. acknowledges the support through a fellowship granted by the German Research Foundation (DFG) for proposal NI1834. T. Katase was supported by PRESTO, Japan Science and

Technology Agency (JPMJPR16R1) and Grant-in-Aid for Scientific Scientists B (19H02425) from JSPS.

Figure captions

Fig. 1: (a) The cubic perovskite $SrGeO_3$ crystal structure. (b) Optical micrograph of a cubic $SrGeO_3$ single crystal. (c) The 100 out-of-plane HR-XRD pattern of a cubic $SrGeO_3$ single crystal with the intensity plotted on a logarithmic scale. (d) PBE0-calculated band structure along high symmetry directions in the first Brillouin zone indicates 2.7 eV indirect and 3.4 eV direct band gaps and a large CB dispersion. (e) Reflection ellipsometry spectrum for the evaluation of (f) the absorption coeffient data $\alpha^{1/2}$ and α^2 indicate optical band gaps in agreement with the specular reflectance *R* edge and the calculated values.

Fig. 2: (a) IR reflectance spectrum of a mirror-polished cubic $SrGeO_3$ polycrystalline pellet. (b) Raman scattering spectrum of a cubic perovskite $SrGeO_3$ single crystal. The first-order Raman peaks at 493 cm^{-1} and 742 cm^{-1} provide the LO_2 and LO_3 phonon frequencies in the dispersion model, as given by the maxima of the loss function $-\mathrm{Im}(\varepsilon^{-1})$.

Fig. 3: (a) Real part of ε_1 of the dielectric function of cubic $SrGeO_3$, $BaSnO_3$ and $SrTiO_3$. The LO phonon frequencies correspond to the zeros of ε_1. (b) The maxima of the imaginary part ε_2 of the dielectric function and the loss function $-\mathrm{Im}(\varepsilon^{-1})$ correspond to the frequency of TO and LO phonon modes, respectively. The peak heigths of the TO and LO phonons indicate the magnitude of polarization, but it must be considered that the peak broading due to damping ($\gamma_\mu > 0$) is taken into account.

Fig. 4: Calculated phonon band structures of cubic $SrGeO_3$, $BaSnO_3$ and $SrTiO_3$ obtained by density functional perturbation theory. The 3 IR active TO modes at the Γ point of the first Brillouin zone (empty circles) are schematically illustrated based on the calculated ion displacement vectors. The inactive eigenmodes are indicated with a cross. The LO eigenfrequencies at the Γ point are indicated by the horizontal lines.

Fig. 5: Relaxation time of carrier scattering τ_ν at T = 298 K by LO phonons as a function of the phonon energy $\hbar\omega_{\mathrm{l}_\nu}$ and oscillator strength $\varepsilon_{\mathrm{lv}}$ for cubic (a) $SrGeO_3$, (b) $BaSnO_3$ and (c) $SrTiO_3$, according to Eqs. (5) and (6). The smallest relaxation time among the three LO phonon modes, which is the most crucial for the intrinsic electron mobility, is indicated by the dashed line. The LO peak heigths of the loss function $-\mathrm{Im}(\varepsilon^{-1})$ indicate the magnitude of polarization, but it must be considered that the peak broading due to damping ($\gamma_\mu > 0$) is taken into account.

Fig. 6: IR reflectance spectrum of a mirror-polished, 2 at.% La-doped cubic $SrGeO_3$ ($La_{0.02}Sr_{0.98}GeO_3$) polycrystalline pellet.

References

[1] A. Ohtomo and H.Y. Hwang, Nature **427**, 423 (2004).

[2] J. Mannhart and D.G. Schlom, Science (80-.). **327**, 1607 (2010).

[3] J. Son, P. Moetakef, B. Jalan, O. Bierwagen, N.J. Wright, R. Engel-Herbert, and S. Stemmer, Nat Mater **9**, 482 (2010).

[4] T.A. Cain, A.P. Kajdos, and S. Stemmer, Appl. Phys. Lett. **102**, 182101 (2013).

[5] X. Luo, Y.S. Oh, A. Sirenko, P. Gao, T.A. Tyson, K. Char, and S.-W. Cheong, Appl. Phys. Lett. **100**, 52104 (2012).

[6] H.J. Kim, U. Kim, H.M. Kim, T.H. Kim, H.S. Mun, B.-G. Jeon, K. T.Hong, W.-J. Lee, C. Ju, K.H. Kim, and K. Char, Appl. Phys. Express **5**, 61102 (2012).

[7] U. Kim, C. Park, T. Ha, Y.M. Kim, N. Kim, C. Ju, J. Park, J. Yu, J.H. Kim, and K. Char, APL Mater. **3**, 36101 (2015).

[8] K. Krishnaswamy, L. Bjaalie, B. Himmetoglu, A. Janotti, L. Gordon, and C.G. de Walle, Appl. Phys. Lett. **108**, 83501 (2016).

[9] Y. Wang, W. Tang, J. Cheng, S. Nazir, and K. Yang, Phys. Chem. Chem. Phys. **18**, 31924 (2016).

[10] H. Mizoguchi, T. Kamiya, S. Matsuishi, and H. Hosono, Nat. Commun. **2**, 470 (2011).

[11] T. Hughbanks, J. Am. Chem. Soc. **107**, 6851 (1985).

[12] H. Mizoguchi, H.W. Eng, and P.M. Woodward, Inorg. Chem. **43**, 1667 (2004).

[13] S. James Allen, S. Raghavan, T. Schumann, K.-M. Law, and S. Stemmer, Appl. Phys. Lett. **108**, 252107 (2016).

[14] C.A. Niedermeier, S. Rhode, K. Ide, H. Hiramatsu, H. Hosono, T. Kamiya, and M.A. Moram, Phys. Rev. B **95**, 161202 (2017).

[15] P. Singh, B.J. Brandenburg, C.P. Sebastian, P. Singh, S. Singh, D. Kumar, and O. Parkash, Jpn. J. Appl. Phys. **47**, 3540 (2008).

[16] T.N. Stanislavchuk, A.A. Sirenko, A.P. Litvinchuk, X. Luo, and S.-W. Cheong, J. Appl. Phys. **112**, 44108 (2012).

[17] S. supplementary material at [url].

[18] W. Nunn, A. Prakash, A. Bhowmik, R. Haislmaier, J. Yue, J.M. Garcia Lastra, and B. Jalan, APL Mater. **6**, 66107 (2018).

[19] H. Yoshikawa and S. Adachi, Jpn. J. Appl. Phys. **36**, 6237 (1997).

[20] I. Hamberg and C.G. Granqvist, J. Appl. Phys. **60**, R123 (1986).

[21] H.J. van Daal, J. Appl. Phys. **39**, 4467 (1968).

[22] A. Verma, A.P. Kajdos, T.A. Cain, S. Stemmer, and D. Jena, Phys. Rev. Lett. **112**, 216601 (2014).

[23] K. Krishnaswamy, B. Himmetoglu, Y. Kang, A. Janotti, and C.G. de Walle, Phys. Rev. B **95**, 205202 (2017).

[24] H.J. Kim, U. Kim, T.H. Kim, J. Kim, H.M. Kim, B.-G. Jeon, W.-J. Lee, H.S. Mun, K.T. Hong, J. Yu, K. Char, and K.H. Kim, Phys. Rev. B **86**, 165205 (2012).

[25] W.G. Spitzer, R.C. Miller, D.A. Kleinman, and L.E. Howarth, Phys. Rev. **126**, 1710 (1962).

[26] F.A. Grant, Rev. Mod. Phys. **31**, 646 (1959).

[27] T. Hitosugi, N. Yamada, S. Nakao, Y. Hirose, and T. Hasegawa, Phys. Status Solidi **207**, 1529 (2010).

[28] Z. Galazka, R. Uecker, K. Irmscher, D. Klimm, R. Bertram, A. Kwasniewski, M. Naumann, R. Schewski, M. Pietsch, U. Juda, A. Fiedler, M. Albrecht, S. Ganschow, T. Markurt, C. Guguschev, and M. Bickermann, J. Phys. Condens. Matter **29**, 75701 (2017).

[29] R.J. Terry, N. Combs, C.D. McMillen, S. Stemmer, and J.W. Kolis, J. Cryst. Growth 125529

(2020).

[30] Y. Shimizu, Y. Syono, and S. Akimoto, High Temp. High Press. **2**, 113 (1970).

[31] A. Nakatsuka, H. Arima, O. Ohtaka, K. Fujiwara, and A. Yoshiasa, Acta Crystallogr. Sect. E **71**, 502 (2015).

[32] H.T. Hall, Rev. Sci. Instrum. **31**, 125 (1960).

[33] A. M. Gasanaliev, A. I. Rasulov, B. Yu. Gamataeva, and A. K. Mamedova, Russ. J. Phys. Chem. A **86**, 154 (2012).

[34] C.A. Niedermeier, J. Yamaura, J. Wu, X. He, T. Katase, H. Hosono, and T. Kamiya, ACS Appl. Electron. Mater. (2019).

[35] P.E. Blöchl, Phys. Rev. B **50**, 17953 (1994).

[36] G. Kresse and J. Furthmüller, Phys. Rev. B **54**, 11169 (1996).

[37] G. Kresse and D. Joubert, Phys. Rev. B **59**, 1758 (1999).

[38] J.P. Perdew, M. Ernzerhof, and K. Burke, J. Chem. Phys. **105**, 9982 (1996).

[39] A.A. Mostofi, J.R. Yates, Y.-S. Lee, I. Souza, D. Vanderbilt, and N. Marzari, Comput. Phys. Commun. **178**, 685 (2008).

[40] M. Stapelbroek and B.D. Evans, Solid State Commun. **25**, 959 (1978).

[41] A. Togo and I. Tanaka, Scr. Mater. **108**, 1 (2015).

[42] R.E. Hummel, *Electronic Properties of Materials*, 4th ed. (Springer-Verlag New York, 2011).

[43] W.G. Fateley, *Infrared and Raman Selection Rules for Molecular and Lattice Vibrations: The Correlation Method* (Wiley-Interscience, 1972).

[44] C. Kittel, *Introduction to Solid State Physics*, 7th ed. (New York, Wiley, 1996).

[45] T. Kurosawa, J. Phys. Soc. Japan **16**, 1298 (1961).

[46] G. Irmer, V. V Toporov, B.H. Bairamov, and J. Monecke, Phys. Status Solidi **119**, 595 (1983).

[47] M. V Klein, B.N. Ganguly, and P.J. Colwell, Phys. Rev. B **6**, 2380 (1972).

[48] A.B. Kuzmenko, Rev. Sci. Instrum. **76**, 83108 (2005).

[49] A. Grzechnik, P.F. McMillan, and W. Petuskey, MRS Proc. **398**, 501 (1995).

[50] A. Grzechnik, H. Hubert, P. Mcmillan, and W. Petuskey, Integr. Ferroelectr. **15**, 191 (1997).

[51] A. Grzechnik, A.V.G. Chizmeshya, G.H. Wolf, and P.F. McMillan, J. Phys. Condens. Matter **10**, 221 (1998).

[52] M. Gajdoš, K. Hummer, G. Kresse, J. Furthmüller, and F. Bechstedt, Phys. Rev. B **73**, 45112 (2006).

[53] D.M. Eagles, J. Phys. Chem. Solids **25**, 1243 (1964).

[54] D.M. Eagles, J. Phys. Chem. Solids **26**, 672 (1965).

[55] K. Tsuda and M. Tanaka, Acta Crystallogr. Sect. A **51**, 7 (1995).

[56] W. Zhong, R.D. King-Smith, and D. Vanderbilt, Phys. Rev. Lett. **72**, 3618 (1994).

[57] H.P.C. Miranda, http://henriquemiranda.github.io/phononwebsite/phonon.html.

[58] B.G. Kim, J.Y. Jo, and S.W. Cheong, J. Solid State Chem. **197**, 134 (2013).

[59] J.D. Axe, Phys. Rev. **157**, 429 (1967).

[60] H. Fröhlich, Adv. Phys. **3**, 325 (1954).

[61] F.E. Low and D. Pines, Phys. Rev. **98**, 414 (1955).

[62] A.K. Prodjosantoso, Q. Zhou, and B.J. Kennedy, J. Solid State Chem. **200**, 241 (2013).

[63] L. Cao, E. Sozontov, and J. Zegenhagen, Phys. Status Solidi **181**, 387 (2000).

[64] M. Ahrens, R. Merkle, B. Rahmati, and J. Maier, Phys. B **393**, 239 (2007).

[65] T. Arai, S. Iimura, J. Kim, Y. Toda, S. Ueda, and H. Hosono, J. Am. Chem. Soc. **139**, 17175 (2017).

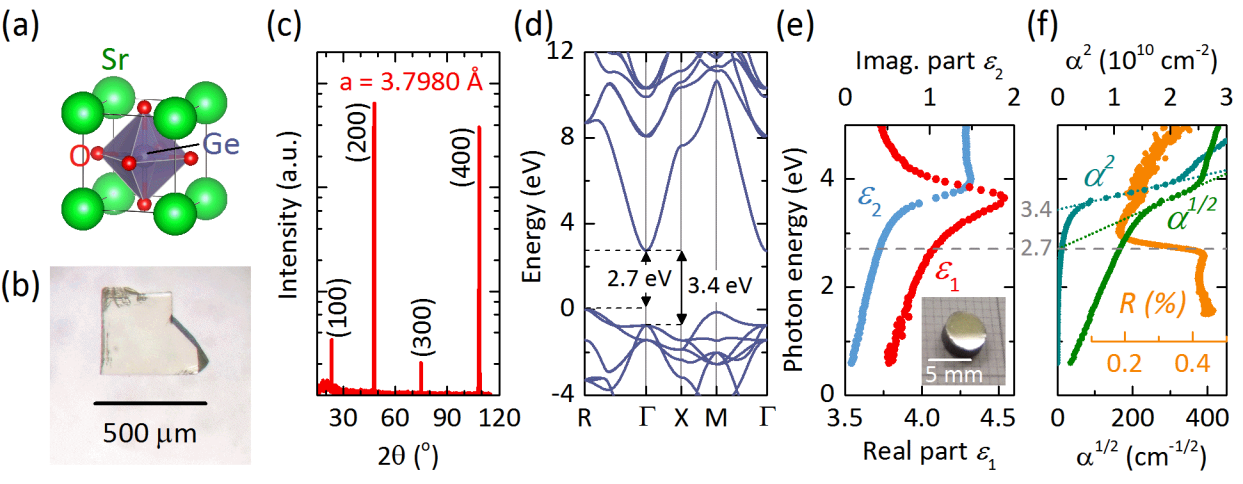
(a)
Sr
O
Ge
(b)
500 μm
(c)
a = 3.7980 Å
(200)
(400)
(100)
(300)
Intensity (a.u.)
30
60
90
120
2θ (°)
(d)
12
8
4
0
-4
Energy (eV)
2.7 eV
3.4 eV
R
Γ
X
M
Γ
(e)
Imag. part ε2
0
1
2
Photon energy (eV)
4
2
0
ε2
ε1
5 mm
3.5
4.0
4.5
Real part ε1
(f)
α2 (10^10 cm^-2)
0
1
2
3
α2
α1/2
3.4
2.7
R (%)
0.2
0.4
0
200
400
α1/2 (cm^-1/2)

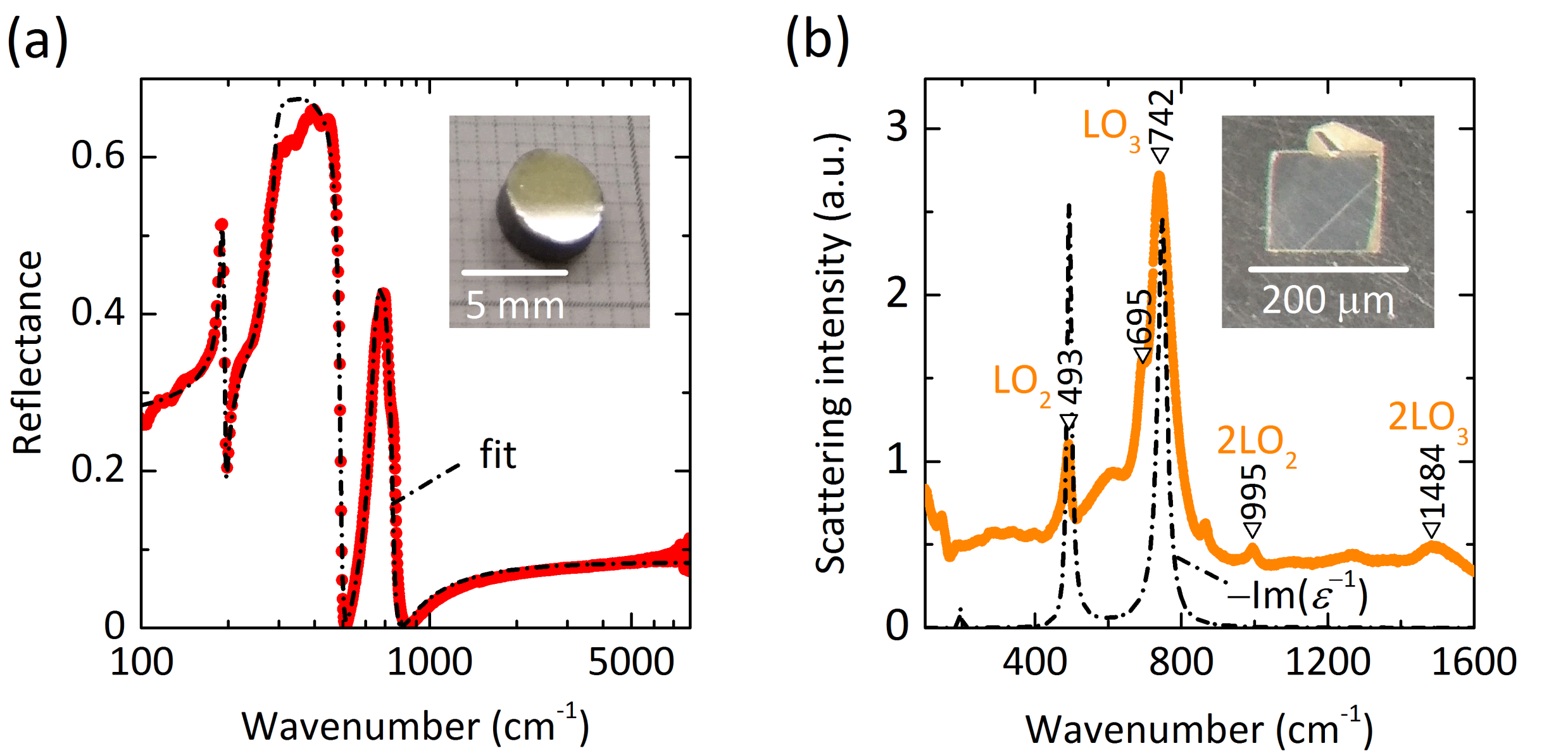
(a)
Reflectance
0
0.2
0.4
0.6
100
1000
5000
Wavenumber (cm-1)
fit
5 mm
(b)
Scattering intensity (a.u.)
0
1
2
3
400
800
1200
1600
Wavenumber (cm-1)
LO2
493
LO3
742
695
2LO2
995
2LO3
1484
−Im(ε−1)
200 μm

(a)

SrGeO$_3$

196 LO$_1$

493 LO$_2$

748 LO$_3$

BaSnO$_3$

146

425

720

SrTiO$_3$

174

461

816

Real part ε_1

Wavenumber (cm^{-1})

(b)

SrGeO$_3$

TO$_1$

TO$_2$

TO$_3$

LO$_1$

LO$_2$

LO$_3$

x10

BaSnO$_3$

ε_2

-Im(ε^{-1})

x10

SrTiO$_3$

x100

Imaginary part ε_2

Loss function -Im(ε^{-1})

Wavenumber (cm^{-1})

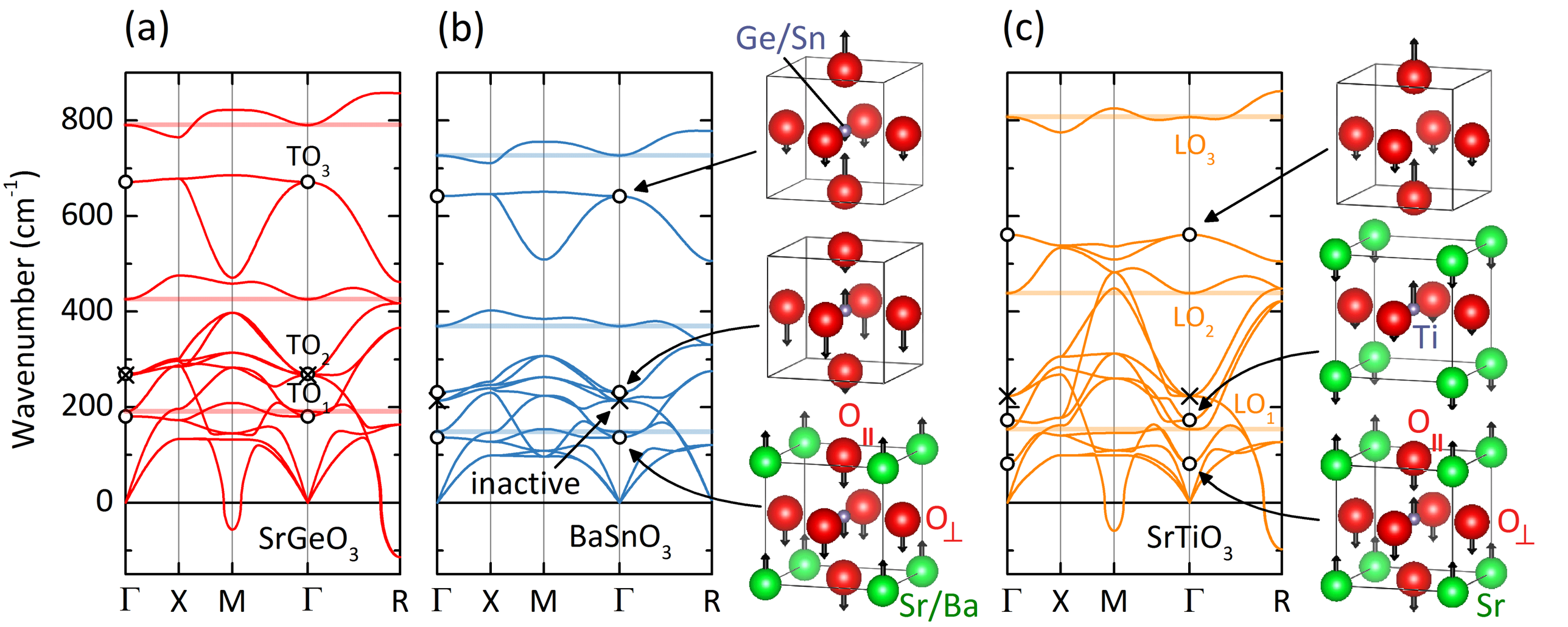
(a)
(b)
(c)
Wavenumber (cm^{-1})
800
600
400
200
0
TO$_3$
TO$_2$
TO$_1$
SrGeO$_3$
inactive
BaSnO$_3$
Ge/Sn
O$_{II}$
O$_\perp$
Sr/Ba
LO$_3$
LO$_2$
LO$_1$
SrTiO$_3$
Ti
O$_{II}$
O$_\perp$
Sr
Γ X M Γ R
Γ X M Γ R
Γ X M Γ R

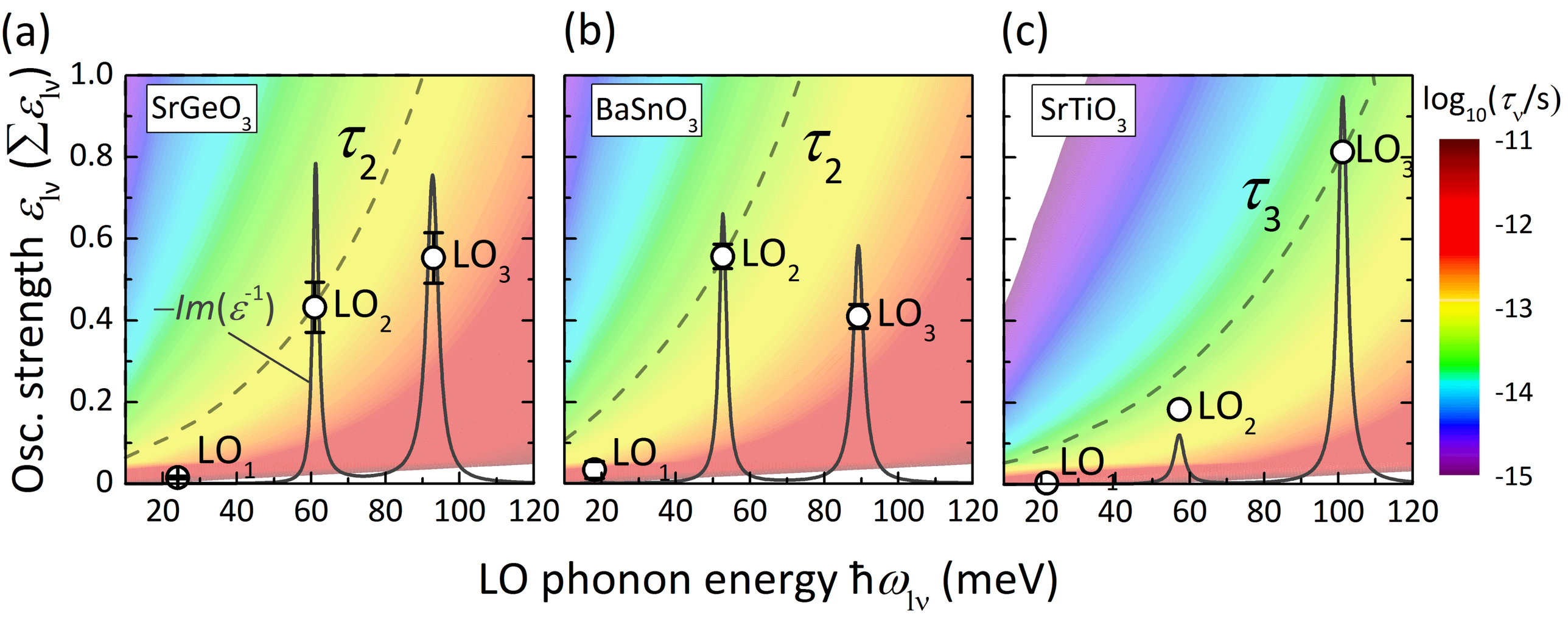
(a)
(b)
(c)
SrGeO3
BaSnO3
SrTiO3
τ2
τ3
LO1
LO2
LO3
−Im(ε-1)
Osc. strength εlν (∑εlν)
LO phonon energy ħωlν (meV)
log10(τν/s)
-11
-12
-13
-14
-15
0
0.2
0.4
0.6
0.8
1.0
20
40
60
80
100
120

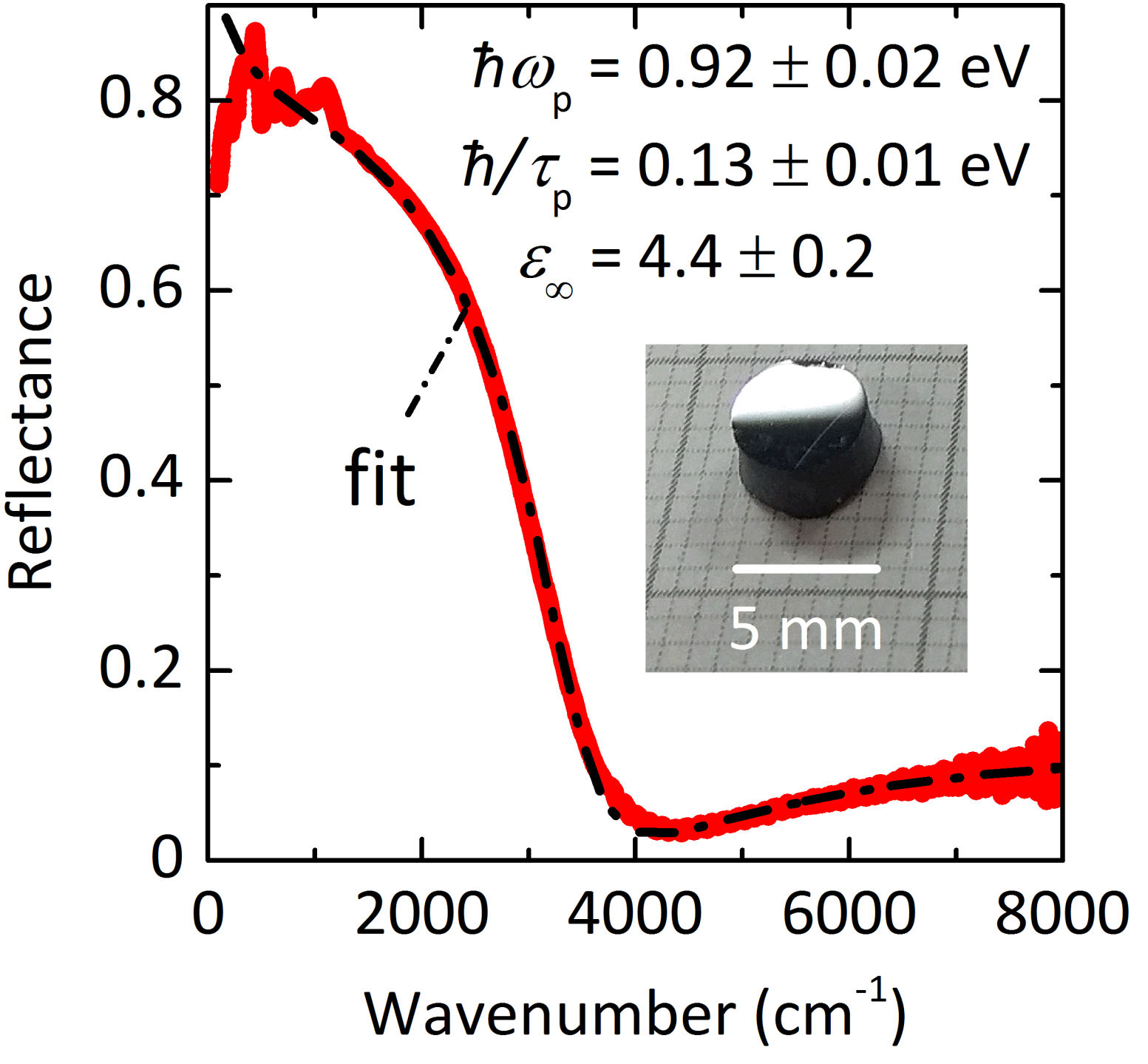
$\hbar\omega_p = 0.92 \pm 0.02$ eV
$\hbar/\tau_p = 0.13 \pm 0.01$ eV
$\varepsilon_\infty = 4.4 \pm 0.2$
fit
5 mm
Reflectance
0
0.2
0.4
0.6
0.8
0
2000
4000
6000
8000
Wavenumber (cm^{-1})